Steel and Composite Structures, *Vol. 34, No. 1* (*2020*) *35-51*
DOI: https://doi.org/10.12989/scs.2020.34.1.035

Low-cycle fatigue in steel H-piles of integral bridges; a comparative study of experimental testing and finite element simulation

Memduh Karalar[1] and Murat Dicleli[*2]

[1]*Department of Civil Engineering, Bülent Ecevit University, Zonguldak, Turkey*
[2]*Department of Engineering Sciences, METU, 06800 Ankara, Turkey*

(*Received May 10, 2019, Revised October 12, 2019, Accepted October 15, 2019*)

Abstract. Integral abutment bridges (IABs) are those bridges without expansion joints. A single row of steel H-piles (SHPs) is commonly used at the thin and stub abutments of IABs to form a flexible support system at the bridge ends to accommodate thermal-induced displacement of the bridge. Consequently, as the IAB expands and contracts due to temperature variations, the SHPs supporting the abutments are subjected to cyclic lateral (longitudinal) displacements, which may eventually lead to low-cycle fatigue (LCF) failure of the piles. In this paper, the potential of using finite element (FE) modeling techniques to estimate the LCF life of SHPs commonly used in IABs is investigated. For this purpose, first, experimental tests are conducted on several SHP specimens to determine their LCF life under thermal-induced cyclic flexural strains. In the experimental tests, the specimens are subjected to longitudinal displacements (or flexural strain cycles) with various amplitudes in the absence and presence of a typical axial load. Next, nonlinear FE models of the tested SHP specimens are developed using the computer program ANSYS to investigate the possibility of using such numerical models to predict the LCF life of SHPs commonly used in IABs. The comparison of FE analysis results with the experimental test results revealed that the FE analysis results are in close agreement with the experimental test results. Thus, FE modeling techniques similar to that used in this research study may be used to predict the LCF life of SHP commonly used in IABs.

Keywords: Integral Abutment Bridge; Steel H-Pile; Low Cycle Fatigue; finite element simulation

1. Introduction

Integral abutment bridges (IABs) are those bridges with no expansion joints where the superstructure is built monolithically with the abutments. The abutments are generally built as thin and short and are supported by a single row of steel H-piles (SHPs) to form a flexible support system at the bridge ends to accommodate thermal-induced displacements of the bridge. Consequently, as the IAB expands and contracts due to temperature variations, the SHPs supporting the abutments are subjected to cyclic lateral (longitudinal) displacements (Fig. 1). The elongation and shortening of the IAB produces one large cyclic longitudinal displacement and associated flexural strain in the SHPs at the abutments each year due to seasonal temperature variations (summer and winter) and several smaller cyclic longitudinal displacements (or flexural strains) due to short-term temperature variations as verified by field-testing of a number of IABs (Dicleli and Albhaisi 2004, Xiao *et al*. 2006, Frosch *et al*. 2006, Chocichien 2004, Karthigeyan 2006). A typical SHP longitudinal displacement versus time record is shown in Fig. 2. Such longitudinal cyclic displacements and associated flexural strains induced by thermal elongation and contraction of the bridge may eventually lead to low-cycle fatigue (LCF) failure of the piles. For this reason, the prediction of the LCF life of SHPs at the abutments is essential especially in the design of long IABs, where thermal-induced displacements and associated flexural strains are large.

Although bridge engineers have already predicted that LCF may occur in the SHPs of IABs due to thermal effects (Dicleli 2000, Dicleli and Albhaisi 2004, French *et al.* 2004 and Hällmark 2006), only a few research studies and experimental test results on LCF life of SHPs are available in the literature. Moreover, in most bridge design specifications such as AASHTO (American Association of State Highway and Transportation Officials) (AASHTO 2007), although fatigue in superstructure members such as steel girders is covered, (Hällmark 2006), LCF in the SHPs of IABs is not yet included in the design specifications. As it is not practical to conduct project-specific experimental LCF tests of SHPs and as such tests are very time consuming and tedious, the use of simulation tools become important in estimating the LCF life of SHPs at the abutments of IABs.

One of the most popular simulation tools in structural and bridge engineering is to employ finite element (FE) modeling techniques to simulate the complex behavior of structural components under various loading conditions. Such techniques may also be used to predict the LCF life of SHPs at the abutments of IABs. However, experimental verifications of such simulation techniques is essential to prove their reliability. In this paper, the potential of using

∗Corresponding author, Professor
E-mail: mdicleli@metu.edu.tr

http://www.techno-press.org/?journal=scs&subpage=6
ISSN: 1229-9367 (Print), 1598-6233 (Online)

FE modeling techniques to estimate the LCF life of SHPs commonly used in IABs is investigated. For this purpose, first, experimental tests are conducted on several SHP specimens to determine their LCF life under thermal-induced cyclic flexural strains. In the experimental tests, only the effect of cyclic displacements (or flexural strains) due to seasonal temperature variations are considered as such cyclic displacements are known to induce the most LCF damage in the SHPs (Karalar and Dicleli 2016). Accordingly, the SHP specimens are subjected to seasonal cyclic longitudinal displacements (or flexural strains) with various amplitudes in the absence and presence of a typical axial load. Next, nonlinear FE models of the tested SHP specimens are developed using the computer program ANSYS (ANSYS 1998) to investigate the possibility of using such FE models to predict the LCF life of SHPs commonly used in IABs. As an outcome of this research study, the effect of various important parameters such as cyclic strain amplitude and axial load on LCF life of SHPs is explored and it is shown that FE models may be used to avoid the huge cost and testing time required for conducting experimental tests to estimate the LCF life of SHPs in IABs.

2. Literature review

There are a number of research studies on the effect of thermal loading on the performance of IABs (Dicleli and Albhaisi 2004, French *et al.* 2004, Hällmark 2006, Karalar and Dicleli 2016, Azamfar and Moshrefifar 2014, Arsoy *et al.* 2002).

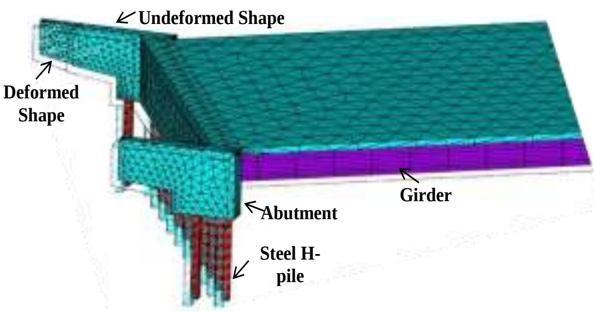

Fig. 1 Pile displacement due to thermal changes

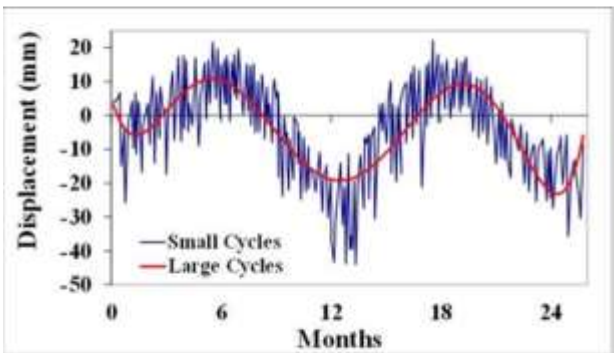

Fig. 2 Pile longitudinal displacement vs. time Girton *et al*. (1991)

However, research studies making a comparison between FE model and experimental test results on the LCF performance of SHPs at the abutments of IABs under the effect of thermal-induced cyclic strains have not been found in the literature. Followings are the results of literature review on FE simulation of IAB or SHP behavior:

Huang *et al.* (2004) investigated the behavior of concrete IABs through field-testing followed by a numerical parametric study. A 3D FE model of the test bridge taking into account soil-structure interaction was developed. The model was calibrated using data collected from the field tests under the effect of the seasonal and more frequent temperature variations. Then, using the developed FE model, a parametric study was conducted to extend the results of the test bridge to other IABs with different design variables including pile type, bridge span and length as well as wing-wall length and orientation.

In another study performed by Khodair and Hassiotis (2005), a 3-D non-linear FE model of an IAB was developed to study the effect of thermal loading on the soil-pile system. In the research study, the pile longitudinal displacements induced by thermal elongation and contraction were measured and then used as an input to the FE model. Then, the results from the FE analyses were compared to measured displacements/strain data. The results obtained from the FE model compared very favorably to those measured using the data acquisition system.

Experimental tests performed by Xiao and Chen (2013) were used to investigate the behavior of a new anchor detail of SHPs connected to a reinforced concrete pile cap where anchor bars are welded to the web of the SHP specimen. Xiao and Chen 2013) also performed FE modeling and analyses of the SHP anchor detail and compared the results with those from the experimental tests. It was observed that the FE model is capable of simulating the experimental behavior of the tested SHP specimen and reinforced concrete pile-cap connections.

Khodair and Hassiotis (2013) presented findings of the numerical and experimental study of the Scotch Road IAB located in Trenton, NJ, USA. First, the bridge substructure was fully instrumented, and data on piles and other structural members were collected. Next, 3-D nonlinear FE model of the full bridge was developed and calibrated with the field measurement data to study the effect of thermal loading on the bridge substructure. The results obtained from the FE model compared reasonably well with the field measurement data.

In another research study performed by Razmi *et al.* (2014) a 3-D nonlinear FE model of a bridge was constructed using the computer program ANSYS (ANSYS 1998) to study the behavior of piles in IABs under seasonal and daily thermal loading. The model was parametrically run for five different bridge lengths that varied from 122 to 549 m. Then, the results from FE model were compared to those from experimental measurements available in the literature regarding the development of plastic strain in the piles as well as the pile behavior in these structures. The research study revealed that nonlinear, 3D FE analysis of the IABs provided a qualitative verification of experimental

Table 1 Dimensions of SHPs

Designation	Pile Weight (Kg/m)	Total Area ($10^3 mm^2$)	Depth (mm)	Flange		Web	
				Width (mm)	Thickness (mm)	Depth (mm)	Thickness (mm)
HP 220x57	57.2	7.29	210	245	11.0	188	11.0
HP 260x57	75	9.55	249	265	12.0	225	12.0

Table 2 Section properties of SHPs

Designation	Axis X-X				Axis Y-Y			
	I_x ($10^6 mm^4$)	S_x ($10^3 mm^3$)	r_x (mm)	Z_x ($10^3 mm^3$)	I_x ($10^6 mm^4$)	S_y ($10^3 mm^3$)	R_y (mm)	Z_y ($10^3 mm^3$)
HP 220x57	57.29	545	88	613	20.7	185.2	53.4	285
HP 260x57	106.5	855	105	958	37.3		62.5281.7	435

measurements available in the literature.

Based on the above discussions, it is clear that FE modelling approach has a great potential of simulating the actual behavior of IABs or IAB components. Thus, such an approach may also be used to study the LCF performance of SHPs at the abutments of IABs subjected to cyclic thermal-induced displacements. However, the accuracy of FE modeling approach to simulate the LCF performance of SHPs in IABs needs to be confirmed by experimental testing. If the FE simulation is proven effective, it may be used to avoid the huge cost and testing time required for conducting experimental tests to estimate the LCF life of SHPs in IABs. FE simulation may also be used to conduct a parametric study to explore the effect of various parameters on the LCF life of SHPs in IABs.

3. Research objective, scope and methodology

The main objective of this research study is to simulate the LCF performance of SHPs at the abutments of IABs under thermal-induced cyclic displacements via FE approach and to demonstrate the capability of such an approach for predicting the LCF life of SHPs via experimental testing.

The scope of this research study is limited to commonly used non-compact SHPs oriented to bend about their strong axis. In this type of SHPs, local buckling of the web or flanges is expected to occur under cyclic longitudinal displacements and this phenomenon is considered in this research study.

To achieve the above-stated objective, first, experimental studies on full-scale non-compact SHP specimens are conducted to determine their LCF life under cyclic flexural strains. In the experimental study, HP220x57 and HP260x75 pile sections are used. These sections are selected based on their common use as IAB piles as well as their availability from the steel manufacturer. Tables 1 and 2 display the dimensions and section properties of the SHPs used in this study.

The specimens are then subjected to longitudinal displacements (or flexural strain cycles) with various amplitudes in the absence and presence of a typical axial load to determine their LCF life. Then, nonlinear FE models of the SHP specimens are developed using the program ANSYS (ANSYS 1998) to numerically predict their LCF life under the same cyclic displacements used in experimental testing. Next, the FE analyses results are compared with those from experimental testing to measure the accuracy of FE simulation in predicting the LCF life of SHPs subjected to thermal-induced cyclic flexural strains.

4. Test setup

4.1 Description of the test set-up

As mentioned earlier, due to thermal fluctuations, the abutment-pile system in an IAB is displaced horizontally producing bending moment in the abutment piles. Earlier research studies show that the maximum bending moment occurs at the SHP top and there is a point where the moment becomes zero at a certain distance below the abutment (Dicleli and Albhaisi 2004, Huang *et al.* 2004) (Fig. 2). The length, Le, of the SHP from the abutment bottom to the point of zero moment is known as the equivalent pile length (EPL) (Fig. 2(b)). Accordingly, in the experimental testing, a simple inverted-cantilever test set-up is used to mimic the upside down geometry of the pile-abutment system of an IAB. The length of this inverted-cantilever is equal to Le, as described in Fig. 3 where Le is measured from the load application point to the top of the steel base fixture (SBF) used to provide fixity to the pile as in the case of the abutment. The SBF is composed of a steel box encasing the SHP specimen with hole dimensions nearly identical to the outside rectangular perimeter of the SHP section. The cavity between the flanges, web and the SBF is filled by a steel block to ensure uniform stress/strain distribution as in the case of concrete encasement. It is noteworthy that a reinforced concrete fixture simulating the integral abutment is not used in the tests due to possible

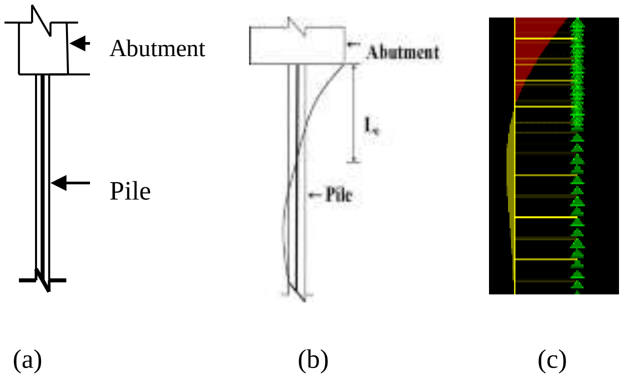

Fig. 2 (a) Typical abutment-pile system of an IAB, (b) Moment distribution along the length of the pile under thermal-induced longitudinal pile displacement and the and (c) The obtained from pushover analyses results as depicted on the FE model

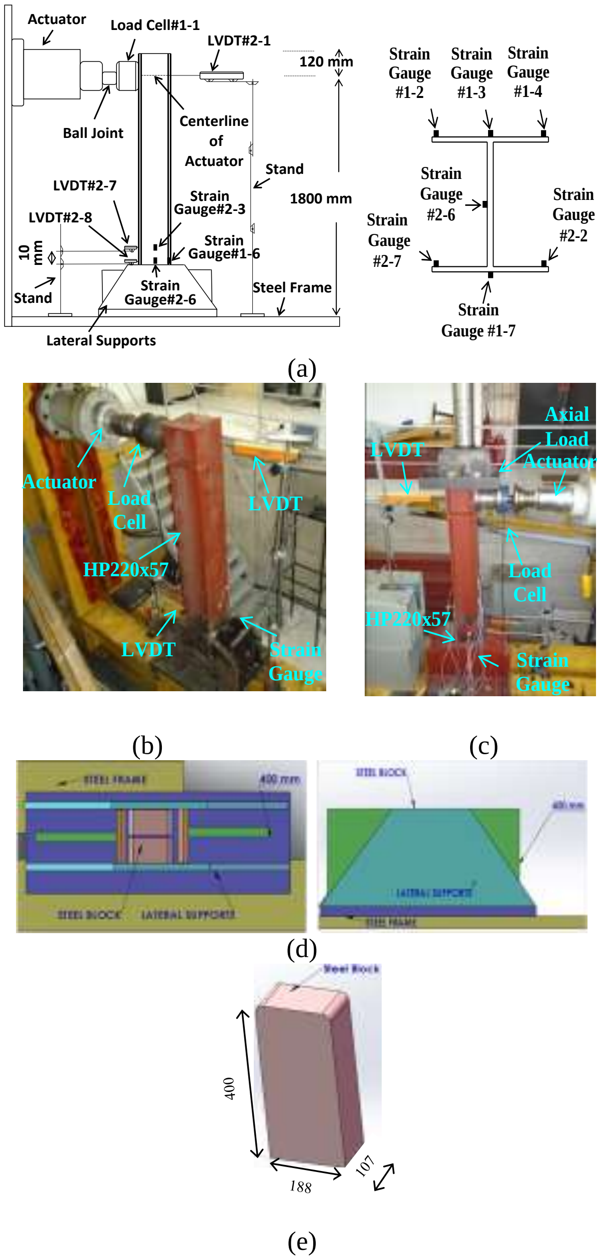

Fig. 3 (a) Schematic plot of the test set-up: depicting the location of the strain gauges and LVDT, Photograph of the test set up, (b) without axial load, (c) with axial load, (d) details of SBF (top and side views) and (e) details of steel block damage and cracking of concrete upon cyclic loading, which may lead to loosening of the SHP-abutment connection (Azamfar *et al*. 2014, Arsoy *et al.* 2002, Huang *et al*. 2004) and as a result, the correct measurement of SHP strains may become impossible. The SBF is connected to the rigid test frame and the cyclic displacement is applied to the top of the cantilever pile specimen as shown in Fig.3. HP220x57 and HP260x75 SHP specimens are tested to determine their LCF life under cyclic flexural strains.

To determine the length, Le, of the tested SHP specimens, nonlinear structural models of two typical IABs with four different types of soft to stiff foundation soils are build using the program SAP 2000 (SAP2000 2016). The bridge abutments are assumed to be supported by HP220x57 and HP260x75 piles as used in the tests. More details about the bridges and bridge models are given in (Dicleli and Albhaisi 2004). 128 static pushover analyses of the IAB models simulating longitudinal thermal deformation of the bridges and the piles are then conducted to obtain the moment diagram of the SHPs for various foundation soil conditions. From the pile moment diagrams obtained from the analyses, the location of the point of zero moment is determined (Fig. 2(c)). The length of the pile measured from the abutment bottom to the point of zero moment is the EPL, Le. The average of the EPLs obtained from all the 128 static pushover analyses is taken as the EPL of the pile specimens used in the tests. Based on the pushover analyses results, the EPL is determined as 1350 mm. The total length of each pile specimen used in the tests is taken as 1900 mm, where the 400 mm segment of the specimen is encased in the SBF to provide fixity and the load is applied at 150 mm from the top of the specimen. Moreover, prior to testing, the FE model of a typical SHP specimen together with the SBF is built (Fig. 4). In the FE model, both the loading and boundary conditions of the test are simulated. FE analysis of the model is then conducted; (i) to identify the appropriate locations of the strain gauges, (ii) to identify possible problems that may occur during testing, and (iii) to improve the test set-up if needed. Based on the FE analyses results, the tests-set-up is slightly modified to eliminate the stress concentrations at the interface of the SBF and the SHP specimen and then, the analyses are repeated to determine the appropriate locations of the strain gauges. Details of the instrumentation are given in the following section.

4.2 Instrumentation of pile specimens and application of axial load and displacement cycles

The SHP specimens are instrumented using three types of measuring equipment as follows (Fig. 3); a load cell, strain gauges (12 of them) and displacement transducers (three of them). Additionally, an actuator with displacement-control having a ±500 kN longitudinal load and a ± 125 mm displacement capacity is used to exert cyclic displacements at the pile top as shown in Fig. 3(b). Moreover, an actuator with force control having a 1000 kN load capacity is used to apply axial load at the top of the pile specimens (Fig. 3(c)).

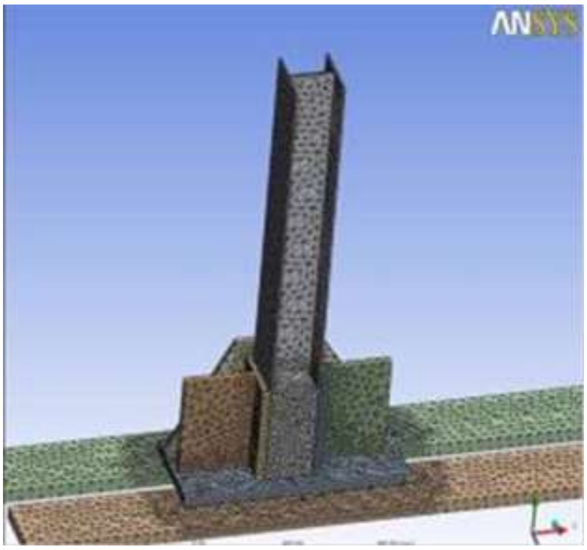

Fig. 4 Finite element simulation of the experimental test set-up

The strain gauge arrangement on the SHP cross-section is shown in Fig. 3(a). Flexural strains at critical locations need to be measured to relate the LCF life of the SHP to the cyclic flexural strain amplitude. Accordingly, flexural strains are measured at critical locations where LCF cracks are expected to occur according to the analyses results of the finite element model of the test set-up (Fig. 4). The longitudinal load, displacements and flexural strains data are processed by a TDG-Ai8b model data-logger and stored on a computer hard-disk connected to the device.

In the tests, the SHP specimens are subjected to cyclic longitudinal displacements with constant amplitude. The SHP specimens are forced to bend about their strong axis using the displacement-controlled actuator mentioned above. The actuator is programmed to operate with a sinusoidal cyclic displacement waveform at a stroke speed of 2 mm/s (0.5 Hz frequency). Past research studies revealed that at such displacement velocities, the fatigue performance of steel components is not affected (Haliburton 1971, Virdi *et al.* 2000) by the loading/displacement rate. For example, the fatigue endurance limit of low carbon steel specimens tested under 2 and 20 Hz loading rate remained the same (Haliburton 1971). Similarly, in another research study, the loading velocity is found not to affect the LCF performance of steel members and their connections (Virdi *et al.* 2000). Therefore, the 2 mm/s displacement rate used in the tests is appropriate for the purpose of this study.

4.3 Material properties of the pile specimens

The HP220x57 and HP260x75 piles used in the tests are made of S 320 GP steel according to EN 10204. Standard tensile tests on steel coupons extracted from the HP220x57 and HP260x75 sections are carried out consistent with the American Standards for Testing Materials, ASTM (ASTM 2005). Using the tensile test' results, the average value of

Table 3 Experimental test and FE analysis results for HP220x57 and HP260x75 steel sections oriented for strong axis bending

Test number	Section type	Axial load	Strain amplitude (ε_a)	Buckling Wave Length / Amplitude (mm		Number of Cycles to Failure		Percentage Change in Fatigue Life
1	HP 220x57	*P=0*	$5\varepsilon_y$	120/6	118/ 5.7	200	205	2.5
5	HP 260x75	*P=0*	$5\varepsilon_y$	109/ 5.6	110/ 5.4	204	235	13
2	*HP 220x57*	*P=0*	$10\varepsilon_y$	207/ 14.7	209/ 15	152	167	9
6	*HP 260x75*	*P=0*	$10\varepsilon_y$	190/ 13.2	193/ 13.6	147	158	7
3	HP 220x57	$P=0.075P_y$	$5\varepsilon_y$	77/8.8	79/9	351	319	10
4	HP 220x57	$P=0.11P_y$	$5\varepsilon_y$	99/8	101/ 8.3	548	585	6

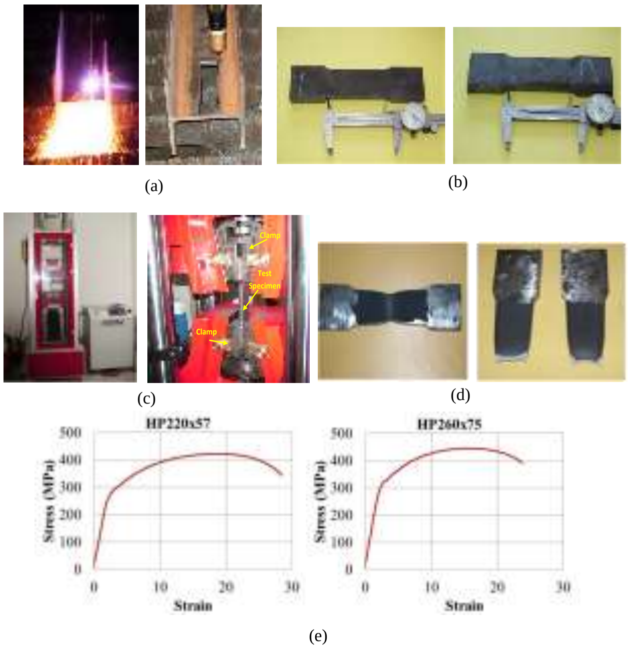

Fig. 5 (a) Cutting process of standart tensile test specimens with CNC method, (b) Tension test specimens for HP220x57 and HP260x75, (c) Tension test machine and soecimen, (d) Tension test specimen after test and (e) Stress-Strain Graph of Tensile Test for HP220x57 and HP260x75

the modulus of elasticity of the steel material is determined as 200,000 MPa, the yield strength is determined as 306 MPa for HP220x57 steel section and 340 MPa for HP260x75 steel section. The ultimate strength is determined as 421 MPa for HP220x57 steel section and 443MPa for HP260x75 steel section. The stress-strain relationships of the SHP specimens obtained from tensile tests are depicted in Fig. 5.

5. Low cycle fatigue tests and summary of test results

In the experimental part of this study, a total of six SHP specimens have been tested under cyclic longitudinal displacements (Fig. 6). Details of the experimental tests and test results are given in Tables 3 and 4. Tests 1-4 are conducted using HP220x57 and HP260x75 SHP sections without axial load and Tests 5 and 6 are performed using HP220x57 SHP sections with axial load equal to 7.5% ($P=0.075P_y$) and 11% ($P=0.11P_y$) of the yield axial load capacity of the SHP specimen respectively.

Table 4 Tensile strain values obtained from experimental tests and FE results or HP220x57 and HP260x75 steel sections oriented to bend about their strong axis

Test number	Strain amplitude (εa)	Experimental Test Results			FE Results		
		Strain Gauge Number			Strain Gauge Number		
		Strain Gauge#1-2	Strain Gauge #1-3	Strain Gauge #1-4	Strain Gauge#1-2	Strain Gauge#1-3	Strain Gauge #1-4
1	$5\varepsilon_y$	*0.0060*	*0.00750*	0.0061	0.00601	0.0076	0.00601
2	$5\varepsilon_y$	*0.0079*	*0.00850*	0.0079	0.00820	0.00853	0.00820
3	$10\varepsilon_y$	*0.0097*	*0.01525*	NA	0.00940	0.01542	0.00940
4	$10\varepsilon_y$	*0.0167*	*0.01700*	NA	0.01680	0.01705	0.01680
5	$5\varepsilon_y$	*0.0082*	*0.00760*	0.0080	0.00822	0.00761	0.00822
6	$5\varepsilon_y$	*NA*	*0.00751*	NA	0.00880	0.00753	0.00880

In all the tests, the fatigue-induced cracks firstly developed at the intersection of the flanges and the web as shown in Fig. 7 (a). The cracks then expanded towards the tips of the flanges under further cycling (Fig 7(a)). Eventually, the fracture occurred right above the 400 mm-high SBF as shown in Fig. 7(b). The fatigue life of the test specimens are estimated as the number of cycles at the moment of complete fracture. Detailed discussions of the tests are given in the following sections.

5.1 Tests 1, 2, 3, 4:

In tests 1 and 2, the piles are subjected to a flexural strain equal to $5\varepsilon_y$ in the outermost fibers of the flanges in each cycle. This required the application of a cyclic longitudinal displacement of ±64 mm and ±97 mm at the top of the HP220x57 (Test 1) and HP260x75 (Test 2) SHP specimens respectively. Fig. 6 shows a typical HP220x57 pile specimen under such a cyclic longitudinal displacement.

Tests 3 and 4 are similar but, the piles are subjected to a flexural strain equal to $10\varepsilon_y$ in the outermost fibers of the flanges in each cycle. This required the application of a cyclic longitudinal displacement of ±90 mm and ±115 mm at the top of the HP220x57 (Test 3) and HP260x75 (Test 4) SHP specimens respectively.

The test results are reported in Table 3. Specimens of tests 1, 2, 3 and 4 fractured due to LCF when the number of cycles reached 200, 204, 152 and 147 respectively. The number of cycles to failure in the case of both HP220x57 (Tests 1 and 3) and HP260x75 (Tests 2 and 4) specimens are observed to be similar for the same flexural strain amplitudes (200 vs 204 and 152 vs 147). This is expected, as the number of cycles to failure is a function of the amplitude of the cyclic strain according to Coffin-Manson relationship (Coffin 1954, Manson 1954). Therefore, the pile size does not affect the LCF life as long as the piles are subjected to the same cyclic strain amplitudes. As the tested SHP specimens are not made of compact sections, in all the cases, local buckling of the flanges of the HP sections occurred with larger local buckling effects at larger cyclic flexural strain amplitudes due to Baushinger effect where the modulus of elasticity of the steel material decreases progressively at each cycle (Dicleli and Calik 2008).

Table 4 presents the tensile strain measurements at the exterior surface of the flange and at three different locations along the flange width (two at the tip of the flange (Strain Gauge #1-2 and 1-4) and one at the junction of the flange and the web (Strain Gauge # 1-3). The strain measurements show that in all the tests, the strain at Strain Gauge # 1-3 is nearly equal to the intended strain level in the test since the reading at this strain gauge was taken as a reference to determine the magnitude of the cyclic longitudinal displacement imposed at the top of the SHP specimen to reach the intended cyclic strain level. The strain measurements at Strain Gauge #1-2 and 1-4 are lower than that of Strain Gauge #1-3. This is mainly due to more bending effect at the junction of the web and flange as the load is transmitted to the base through the web. A slight non-uniform distribution of the strains along the width of the flange may be attributed to the possible sliding and small gaps between the steel block and the SHP specimen. It is noteworthy that as the HP220x57 and HP260x75 sections have different yield strengths (305 MPA for HP220x57 and 340 MPa for HP260x75) and hence different yield strains, the measured and calculated strains at $5\varepsilon_y$ and $10\varepsilon_y$ are also different in magnitude while the strain distribution along the flange width is similar. Further discussion of the tests results will be given in the section where the FE analyses and test results are compared.

(a) (b)

Fig. 6 Application of a cyclic longitudinal displacement at the pile top (a) push and (b) pull direction

(a)

(b)

Fig. 7 (a) Step-by-step spread of fracture throughout the pile flange and (b) Front and side views of fatigue induced steel pile fracture right above the SBF

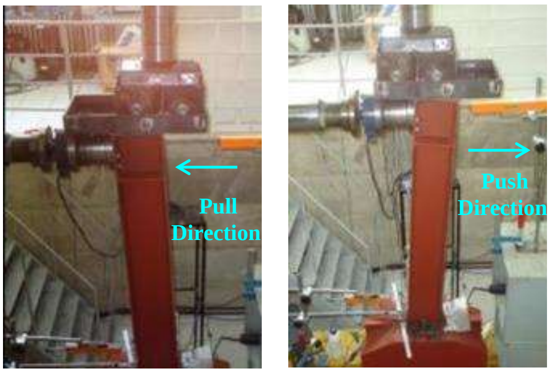

(a) (b)

Fig. 8 Application of cyclic longitudinal displacement at the pile top (a) pull and (b) push direction

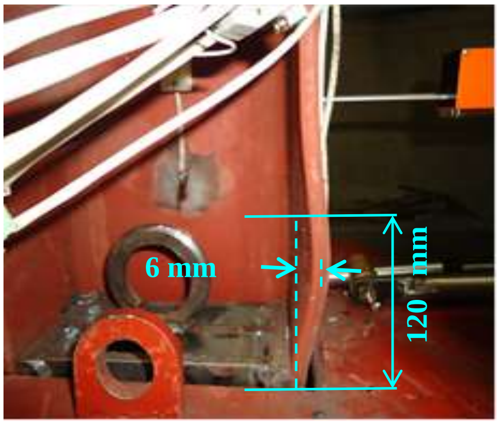

Fig. 9 Local buckling of HP220x57 section for large strain cycles of $\varepsilon_a=5\varepsilon_y$

5.2 Tests 5 and 6

In these tests, flexural strain cycles are applied to the pile specimens in the presence of an axial load. In test 5, an axial load of 170 kN equal to 7.5% of the yield axial strength (P=0.075Py) of the HP220x57 pile specimen is first applied to the pile specimen as shown in Fig. 8. Then, the pile specimen is subjected to large flexural strain cycles equal to $5\varepsilon_y$ in the outermost fibers of the flanges in each cycle. This required the application of a cyclic longitudinal displacement of ±64 mm at the pile top. Test 6 is similar but the HP220x57pile specimen is subjected to an axial load of 250 kN equal to 11% of the yield axial strength ($P=0.11P_y$) of the pile specimen.

The test results are reported in Table 3. The specimens fractured due to LCF when the number of cycles reached 351 and 548 respectively for tests 5 and 6. Similar to tests 1, 2, 3 and 4, local buckling also occurred under cyclic loading in the flanges of the specimens of tests 5 and 6 as shown in Fig. 9. Comparing the results of tests 5 and 6 with that of test 1, it is observed that the number of cycles to failure increased from 200 to 351 for test 5 and 548 for test 6 due to the presence of axial load. The axial load, in these specific cases, has a positive impact on the LCF performance of the SHP. This is expected as the axial load produces axial compressive strains that tend to slow down the fatigue crack propagation due to tensile strains.

Similar to tests 1-4, the strain measurements of tests 5 and 6 are also presented in Table 4. The required cyclic longitudinal displacements at the top of the pile is determined by the reading of Strain Gauge #1-3 when the strain reading is equal to 5εy including the strain generated by the applied axial load (That is, the net tensile strain is equal to 5εy) since the strain due to axial load is quite small and the test procedure would not allow for the precise adjustment of the longitudinal displacement to attain the required strain. The strain measurements show that in all the tests, the strain at Strain Gauge # 1-3 is nearly equal to the intended strain level in the test. This displacement is also used in the FE model. In test 5 (full data is not available for test 6) the strain readings are larger at the tip of the flange than that at the junction of the web and flange. This is mainly due to the more severe local buckling of the flange closer to the tips of the flange due to the presence of the axial load. Further discussion of the tests results will be given in the section where the FE analyses and test results are compared.

6. Finite element modeling

The FE models of the tested SHP specimens and the SBF are built and analyzed under cyclic thermal-induced longitudinal displacements and various levels of axial loads using the program ANSYS (ANSYS 1998). Details of the FE model are described in the following subsections.

6.1. Element types

In the FE modeling, the SHP specimens and their SBF are modeled using 10-node high-order tetrahedron elements with three degrees of freedom at each node. This element is well suited for modeling irregular meshes and contact surfaces (Kamil *et al.* 2011). Accordingly, it is suitable for predicting the surface contact between the SHP and the SBF components and the irregular geometry of the FE model. The contact algorithm of the FE model requires the definition of contact surfaces. Details of the contact surface modeling are given in the following section.

6.2. Contact modeling

In this study, the contact between the SHP specimen and the SBF is defined as a surface-to-surface contact type (Kamil *et al.* 2011, Kadhim 2012). To define a contact surface pairs, one of the surface is designated as a contact element and the other as target element. Both elements need to have the same number of nodes, node locations etc. For the contact interface of the SHP and the SBF, CONTA174 element and a matching TARGE170 element is used to represent contact and separation between the two surfaces (Kamil *et al.* 2011) as shown in Fig. 10.

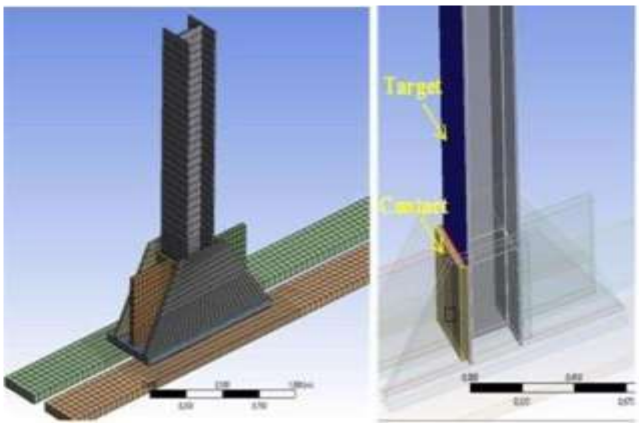

Fig. 10 Details of contact surfaces

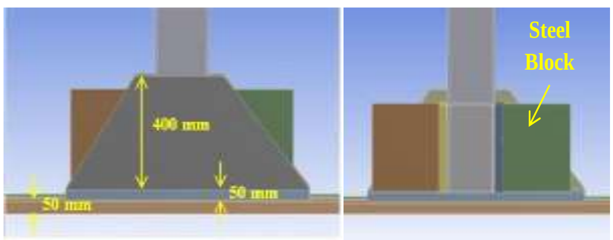

(a)

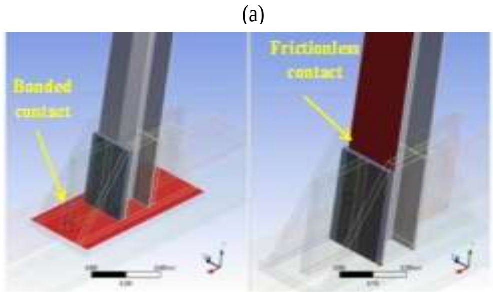

(b)

Fig. 11 (a) Details of SBF and (b) contact type

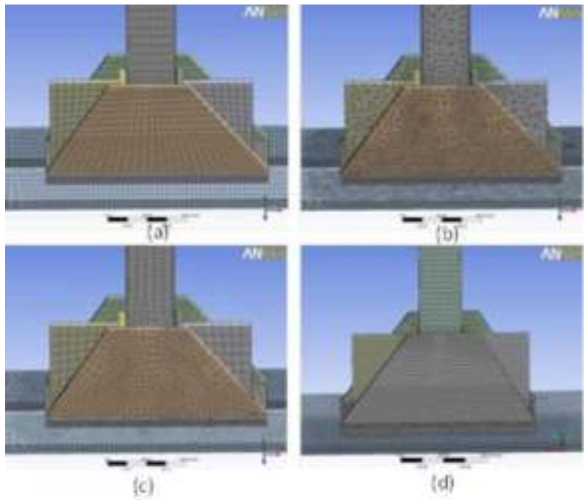

Fig. 12 Mesh options, (a) Automatic Mesh generation, (b) Tetrahedrons Mesh, (c) Hex Dominant Mesh and (d) Sweep Mesh

For the contact area between the flanges of the SHP specimen and the SBF plate, the surfaces are allowed to separate as the longitudinal load is applied on the specimen. Accordingly, frictionless contact is chosen between the HP section and connection plates as gaps form in the model between contacting bodies (Fig. 11). For the remainder of the model, bonded contact is chosen (Fig. 11).

6.3 Meshing

To assure an appropriate mesh density in the FE model, four meshing options are tested and compared: Automatic, Tetrahedrons, Hex Dominant and Sweep meshing options as shown in Fig. 12. The properties of the meshing options are shown in Table 5. As larger number of nodes in a FE model leads to excessive computation time, the Tetrahedrons meshing option is chosen because the obtained mesh has a better size distribution across the FE model and smaller number of nodes. Then, the selected meshing option is tested using various mesh sizes until the results become stable.

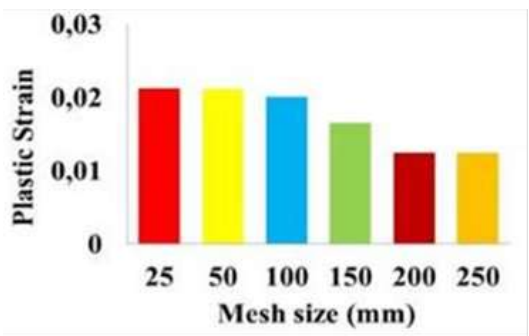

Fig. 13 Strain value for different mesh sizes

Table 5 Numbers of Nodes and Elements for different mesh type

Mesh Type	Number of Nodes	Number of Elements
Tetrahedrons	20207	62303
Automatic	40826	13626
Hex Dominant	47052	16026
Sweep	43922	14658

The largest mesh size giving stable results is then chosen for the FE model. As shown in Fig. 13, the maximum strain value in the HP section remains nearly constant for both 50 mm and 25 mm mesh. Thus, the mesh sizes are input manually and taken as 25 mm within the contact regions and 50 mm within the rest of the model.

6.4. Material model and boundary conditions

In the nonlinear FE model, actual material properties of the SHP specimens are needed to achieve accurate analyses results. Thus, standard tensile tests of steel coupons extracted from the HP sections are performed according to the American Standards for Testing Materials, ASTM (ASTM 2005) to obtain the stress-strain relationship of the steel material and other material properties such as Young's modulus (E), yield (σ_y) and ultimate (σ_u) tensile stresses. Accordingly, the values of σ_y and σ_u used in the FE model are taken as 306 MPa and 421 MPa for the HP220x57 steel section and 340 MPa and 443 MPa for the HP260x75 steel section. A value of 0.3 is used for the Poisson's ratio and 200000 MPa is used for the modulus of elasticity for both HP sections.

Correct definition of the boundary conditions is also important in the FE analysis. The SBFs of the SHP specimens are rigidly connected to the test frame using several rows of high strength bolts. Due to its very large size, the test frame is considered to be rigid compared to the SHP specimens and their SBF. Thus, a fixed boundary condition is used at the bottom of the SBF in the FE element model.

6.5 Low cycle fatigue model

A continuum damage model is used for the estimation of the fatigue life of the SHP specimens due to their ductile behavior (fracture mechanics approach is generally used for brittle materials). Continuum damage modeling approaches have been classified into several groups as stress-based, strain-based, and energy-based approaches. Since the piles in this study experience cyclic plastic deformations and associated low-cycle fatigue, a strain-based fatigue model is selected in ANSYS.

The stain life estimation is based on the Morrow relationship (Suresh 2004, Stephens 2000), which is derived from the superposition of the Coffin–Manson (Coffin 1954, Manson 1954) and Basquin elationships. While the Coffin–Manson relationship correlates the plastic strain amplitude with the number of reversals, the Basquin relationship correlates the elastic strain amplitude with the number of reversals. The Morrow strain life relationship requires four strain-life parameters and two cyclic stress-strain parameters as defined by the following equation

$$\frac{\Delta\varepsilon}{2} = \frac{\sigma_f}{E}\left(2N_f\right)^b + \varepsilon_f\left(2N_f\right)^c \quad (3)$$

Where: $\Delta\varepsilon/2$=total strain amplitude, σ_f=fatigue strength coefficient, E=modulus of elasticity, N_f = number of cycles to failure, $2N_f$ = number of reversals to failure, ε_f =an empirical constant known as the fatigue ductility coefficient, c=an empirical constant known as the fatigue ductility exponent commonly ranging from -0.5 to -0.7 and b=a constant also determined from tests and commonly ranges between -0.098 to -0.262. Fig.14 represents the fatigue resistance information (Eq. (2)) in the form of strain amplitude versus the number of reversals to failure data points for SAE 1045 steel available in ANSYS. The figure presents the experimental elastic, plastic and total strain amplitudes as a function of the number of reversals to failure. The Morrow, Coffin–Manson and Basquin relations are also plotted in the same figure for SAE 1045 steel. The fatigue parameters of this steel type are similar to those of the HP steel sections used in this study and are used to estimate the LCF life of the tested SHP specimens.

7. FE analyses results

FE models of the tested SHP specimens are build and analyzed to estimate their LCF life and to observe the behavior of the SHP specimens such as the effect of axial load, location of the fatigue induced cracks (the location of the fatigue induced cracks from the FE analyses are taken as the location where the maximum plastic strain occurs), local buckling of the flanges including the buckling wave length and amplitude. In the FE model, the axial load and cyclic longitudinal displacements applied on the top of the SHP specimens are kept similar to those in the tests. For example, Fig. 15 shows the deflected shape of the FE model of the SHP specimen in test 3 under longitudinal cyclic displacement.

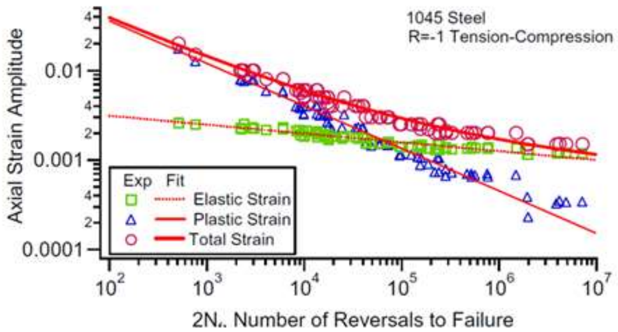

Fig. 14 Total strain amplitudes as a function of the number of reversals to failure for SAE1045 steel

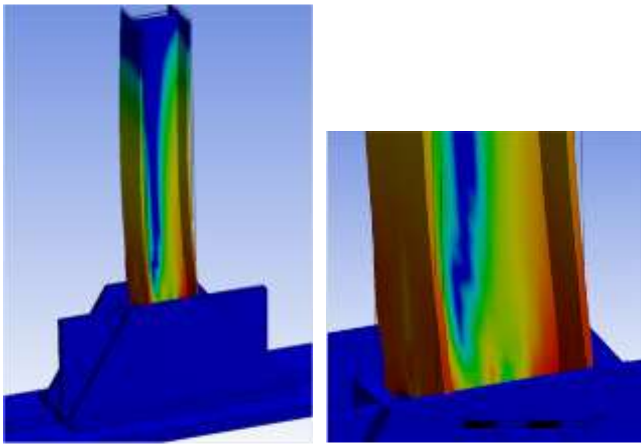

(a) (b)

Fig. 15 HP 220x57 steel specimen under axial and cyclic longitudinal load in FEM (a) Global view and (b) Close-up view at the base

The FE analyses results are then compared with those of the experimental results to assess the capability of FE simulation in capturing the actual behavior of the SHP specimens as observed in the tests. A summary of the FE analysis results are given in the following subsections. More detailed discussion of the FE analyses results will be given when comparing the FE analyses and test results.

7.1 Finite element analysis results of the SHP specimens in tests 1, 2, 3, 4

The FE analyses results for the LCF life of the SHP specimens in tests 1,2,3 and 4 are reported in Table 3. From the FE analyses results, the number of cycles to failure for the SHP specimens in tests 1, 2, 3 and 4 are obtained as 205, 235, 167, and 158 respectively. The equivalent plastic strain distribution in the SHP specimens of tests 1, 2, 3 and 4 are shown in Fig. 16, and the location where the fatigue crack is initiated is shown in Fig. 17. It is observed that the maximum strain occurs at the junction of the web and flange and right above the SBF in all the specimens. The fatigue cracks are also observed to occur at the location of maximum strain in the flanges right above the SBF (Fig. 17). For the SHP specimens of tests 1, 2, 3 and 4, the strains are observed to vary across the flange width from 0.0060 to 0.0076, 0.0082 to 0.00853, 0.0094 to 0.01542, and 0.0168 to 0.017 respectively. The FE analyses results revealed that the number of cycles to failure in the case of tests 1 and 2 as well tests 3 and 4 are similar regardless of the specimen size. That is, for SHPs subjected to the same flexural strain amplitudes, the numbers of cycles to failure are comparable. This is similar to the observations from the experimental test results. Similar to the test results, the FE analyses also yield smaller number of cycles to failure at larger cyclic strain amplitudes. FE analyses also capture the local buckling in the flanges of the FE models of the SHP specimens as shown in Fig. 18. It is observed from the figure that larger local buckling occurs at larger cyclic flexural strain amplitudes (Figs. 18 (a) vs. (b)). The local buckling wave lengths and amplitudes obtained from the FE analyses are tabulated in Table 3. Further discussion of the FE analyses results will be given in the section where the FE analyses and test results are compared.

7.2 Finite element analysis results of the SHP specimens in tests 5 and 6

The FE analyses results for the LCF life of the SHP specimens in tests 5 and 6 are also reported in Table 3. In the FE analyses, in addition to cyclic later displacements, axial loads are also applied at the pile top. From the FE analyses results, the number of cycles to failure for the SHP specimens in tests 5 and 6 are obtained as 319 and 585 respectively.

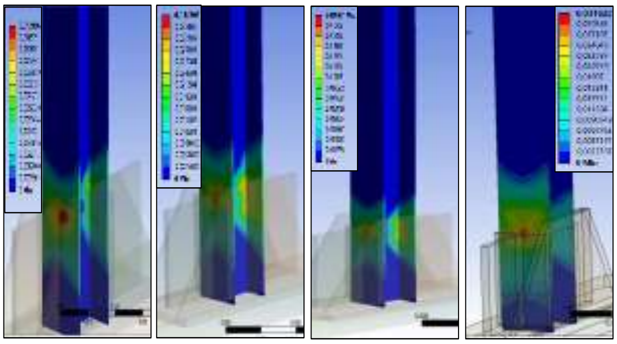

(a) (b) (c) (d)

Fig. 16 Equivalent plastic strain distribution in the SHP specimens of; (a) test 1, (b) test 2, (c) test 3, and (d) test 4

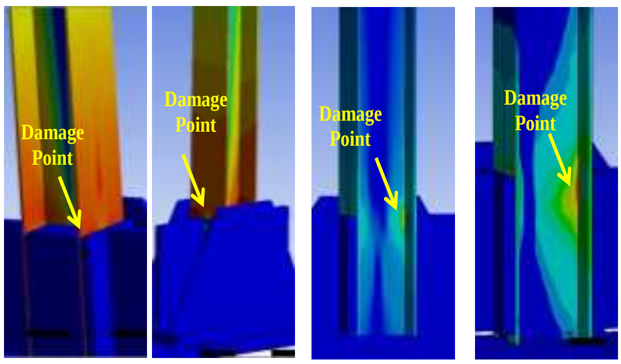

(a) (b) (c) (d)

Fig. 17 The location of the fatigue crack in the SHP specimens of; (a) test 1, (b) test 2, (c) test 3, and (d) test 4

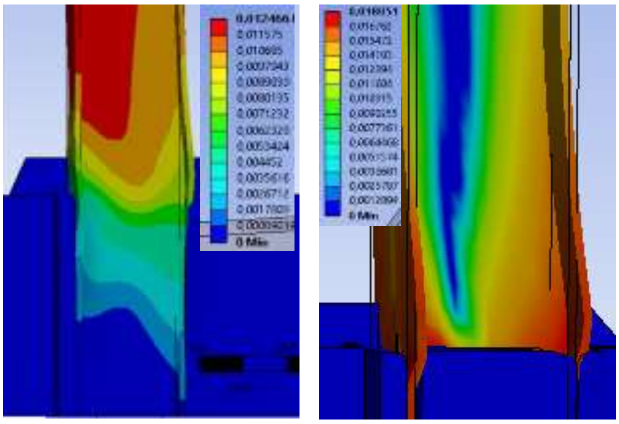

(a) (b)

Fig. 18 Local buckling of the flange; (a) test 1 and (b) test 3

Similar to the experimental test results, FE analyses results revealed that the application of axial load improves the LCF life of the SHP specimen for the εa=5εy cyclic strain amplitude considered in the analyses. That is for the HP220x57 SHP specimen, the number of cycles to failure increased from 205 for P=0 to 319 and 585 for P=0.075Py and P=0.11Py respectively. The equivalent plastic strain distribution in the SHP specimens of tests 5 and 6 are shown in Fig. 19, and the locations of the fatigue cracks are shown in Fig.20. It is observed that the maximum strain occurs at the junction of the web and flange and right above the SBF in all the specimens. As expected, the fatigue cracks occur in the flanges right above the SBF where the strain is maximum. For SHP specimens of tests 5 and 6, the strain is observed to vary across the flange width from 0.0076 to 0.0082 and 0.0073 to 0.00751 respectively. FE analyses also capture local buckling in the flanges of the FE models of the SHP specimens as shown in Fig.20. The local buckling wave lengths and amplitudes obtained from the FE analyses are tabulated in Table 3. Further discussion of the FE analyses results will be given in the section where the FE analyses and test results are compared.

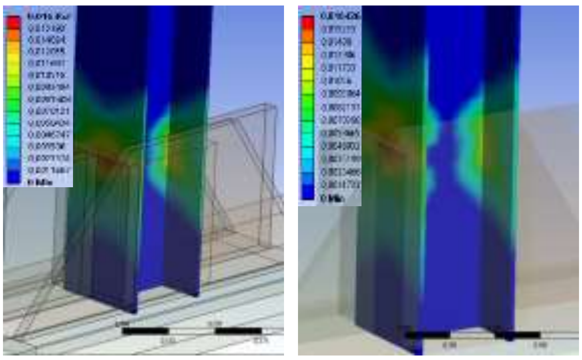

(a) (b)

Fig. 19 Equivalent plastic strain distribution in the SHP specimens of; (a) tests 5 and (b) tests 6

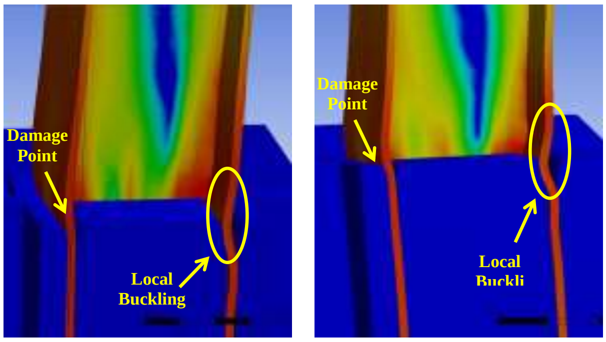

(a) (b)

Fig. 20 The location of the fatigue crack and the crack patterns in the SHP specimens of; (a) tests 5 and (b) tests 6

8. Comparison of FE analyses and experimental test results

In this section, the FE analyses results are compared with those from the experimental testing of the SHP specimens considered in this study. The comparison of the results are based on (i) number of cycles to failure (LCF life), (ii) location of the fatigue crack, (iii) measured strain at various locations of the SHP specimens, (iv) general deformed geometry of the SHP specimens and including flange buckling wave length and amplitude if any. Detailed comparison and discussion of the FE analyses and experimental test results are given in the following subsections.

8.1 SHP Specimens of Tests 1, 2, 3, 4

The experimental test and FE analyses results of the HP220x57 and HP260x75 SHP specimens subjected to cyclic flexural strain with amplitudes of $\varepsilon_a=5\varepsilon_y$ and $\varepsilon_a=10\varepsilon_y$ at the extreme fibers of the flanges are compared. First, the LCF life of the SHP specimens obtained from the experimental tests and FE analyses are compared. First, the monotonic force-displacement (pile top displacement at initial loading) relationship of the SHP obtained from the tests are compared with those of FE analyses in Fig. 21. As observed from the figure a close agreement is found between the test and FE analyses results. In general, within the elastic part, the experimental test results exhibit a slightly smaller initial stiffness, which gradually increases at larger displacements. This is mainly due to the small gaps or movements within the SBF, which are not considered in the FE model. The number of cycles to failure for the SHP specimens obtained from the experimental tests 1, 2, 3 and 4 are 200, 204, 152, and 147 respectively and those obtained from the FE analyses are 205, 235, 167, and 158 respectively. The difference between the LCF life of the SHP specimens obtained from the experimental tests and FE analyses range between 2.5% and 13% and the average of these percentage differences for the four SHP specimens is 7.9%. Thus, the FE model predicted the LCF life of the SHP specimen reasonably well. The location of the fatigue-induced cracks in both the tested SHP specimens and their

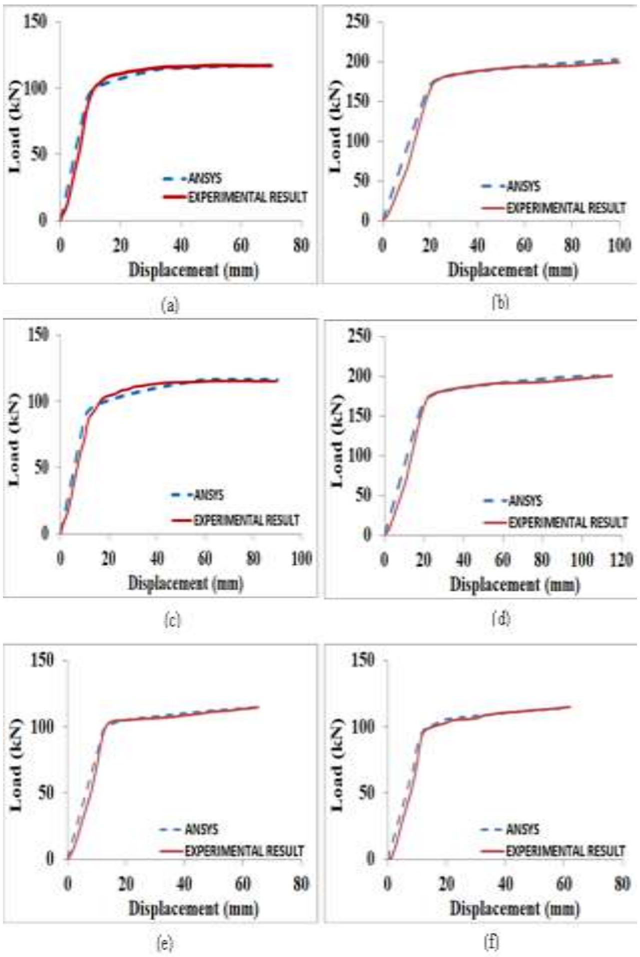

Fig. 21 Comparison of the monotonic force-displacement relationships obtained from FE analyses and experimental test results for; (a) Test 1, (b) Test 2, (c) Test 3, (d) Test 4 (e) Test 5 and (f) Test 6

FE models are shown in Fig. 22 for the SHP specimens in tests 1, 2, 3 and 4. As observed from the figure, in both the experimental tests and the FE models, the fatigue cracks in the SHP specimens occur in the flanges right above the SBF at the location of the maximum flexural strain. Hence, the prediction of the location of LCF induced cracks by the FE model matches those observed from the experimental tests. Table 4 lists the strains from the experimental tests and the FE analyses at various locations (see Fig. 3(a) for the location of strain readings) on the flanges and web of the SHP specimens before the cracks are initiated and the strain readings are steady. The maximum percentage difference between the measured and calculated strains range between 0.26% and 4% and the average of these percentage differences for the four SHP specimens is 2%. Thus, the FE models predicted the strains of the SHP specimens reasonably well. The general deformed geometry of the SHP specimens including flange local buckling from the experimental testing and FE models are compared in Fig.23. The comparison is performed at the instant of maximum longitudinal displacement. As observed from the figure the deformed shapes of the SHP specimens are simulated reasonably well by the FE models of the same specimens. Furthermore, as mentioned earlier, the flanges of the SHP specimens undergo local buckling right above the SBF under cyclic loading. The buckling wave length and amplitude measured at the end of the experimental test are compared with those obtained from FE analyses in Table 3. As observed from the table, the results from the tests and FE analyses agree reasonably well. Fig. 23 also shows the buckled portions of the SHP specimens as captured from the tests and FE analyses. As observed from the figure, the FE predictions of the deformed shape of the SHP specimens near the maximum flexural strain region including the shape of the local buckling wave of the flange is reasonably well.

8.2 SHP Specimens of tests 5 and 6

The experimental test and FE analyses results of the HP220x57 SHP specimens subjected to cyclic flexural strain with amplitude of $\varepsilon_a=5\varepsilon_y$ at the extreme fibers of the flanges in the presence of axial loads of $P=0.075P_y$ (Test 5) and $P=0.11P_y$ (Test 6) are compared. First, the LCF life of the SHP specimens obtained from the experimental tests and FE analyses are compared. The number of cycles to failure for the SHP specimens obtained from the experimental tests 5 and 6 are 351 and 548 respectively and those obtained from the FE analyses are 319 and 585 respectively. The differences between the LCF life of the SHP specimens obtained from the experimental tests and FE analyses are 10% and 6% and the average of these percentage differences for the two SHP specimens is 8%.

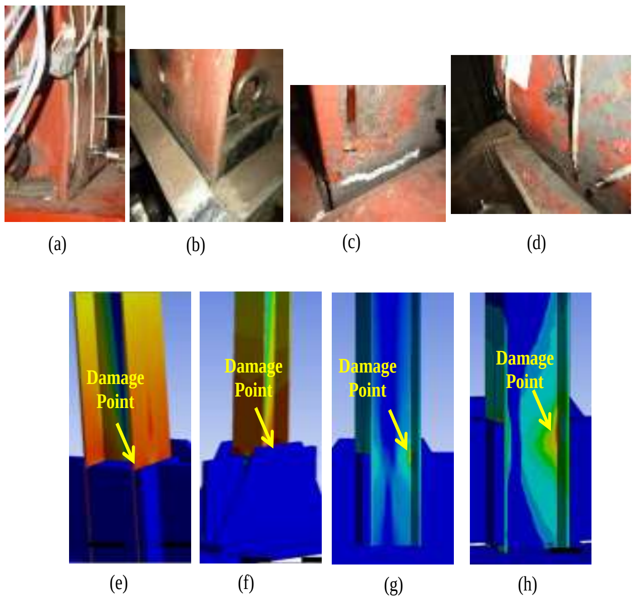

Fig. 22 The location of the fatigue crack in the SHP specimens of; (a) tests 1, (b) tests 2, (c) tests 3, and (d) tests 4 in experimental tests, (e) tests 1, (f) tests 2, (g) tests 3, and (h) tests 4 in FEM

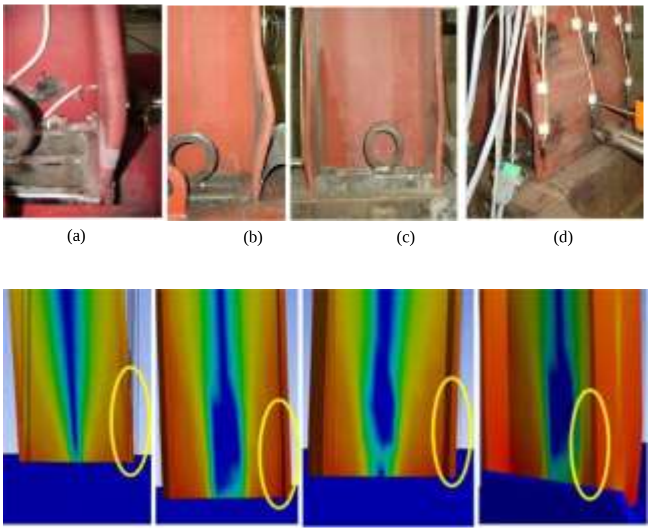

Fig. 23 The local buckling of the SHP specimens of; (a) tests 1, (b) tests 2, (c) tests 3, and (d) tests 4 in experimental tests, (e) tests 1, (f) tests 2, (g) tests 3, and (h) tests 4 in FEM

Thus, the FE model predicted the LCF life of the SHP specimen reasonably well. The location of the fatigue-induced cracks in both the tested SHP specimens and their FE models are shown in Fig. 24 for the SHP specimens in tests 5 and 6. As observed from the figure, in both the experimental tests and the FE models, the fatigue cracks in the SHP specimens occur in the flanges right above the SBF at the location of the maximum flexural strain. Hence, the prediction of the location of LCF induced cracks by the FE model matches those observed from the experimental tests. Table 4 lists the strains from the experimental tests and the FE analyses at various locations (see Fig. 3(a) for the location of strain readings) on the flanges and web of the SHP specimens. The maximum percentage difference between the measured and calculated strains range between 0.4% and 3.2% and the average of these percentage differences for the two SHP specimens is 1.8%. Thus, the FE models predicted the strains of the SHP specimens reasonably well. The general deformed geometry of the SHP specimens including local buckling of the flanges from the experimental testing and FE models are compared in Fig. 25. The comparison is performed at the instant of maximum longitudinal displacement. As observed from the figure the deformed shapes of the SHP specimens are simulated reasonably well by the FE models of the same specimens. Furthermore, as mentioned earlier, the flanges of the SHP specimens undergo local buckling right above the SBF under cyclic loading. The buckling wave length and amplitude measured at the end of the experimental test are compared with those obtained from the FE analyses in Table 3. As observed from the table the results from the tests and FE analyses agree reasonably well. Fig. 25 also shows the buckled portions of the SHP specimens as captured from the tests and FE analyses. As observed from the figure, the FE predictions of the deformed shape of the SHP specimens near the maximum flexural strain region including the shape of the local buckling wave of the flange is reasonably well.

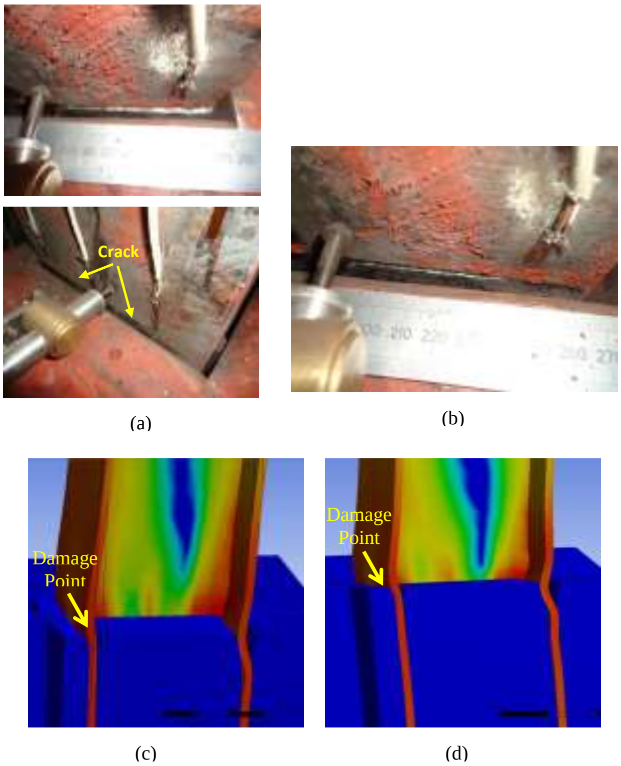

Fig. 24 The location of the fatigue crack and the crack patterns in the SHP specimens of; (a) test 5, (b) test 6 in experimental tests, (c) test 5 and (b) test 6 in FEM

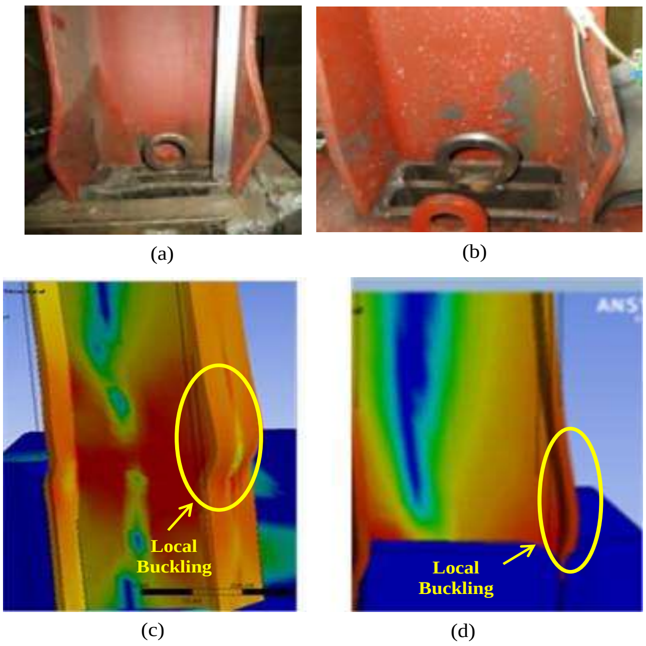

Fig. 25 The local buckling of the SHP specimens of; (a) test 5 and (b) test 6 in experimental test, (c) test 5 and (d) test 6 in FEM

9. Parametric studies using the developed finite element models

In this section, a parametric study is conducted using the FE models of the SHP specimens to obtain a relationship between the LCF life and flexural strain amplitude for various levels of axial loads as well as a relationship between the LCF life and axial load for various levels of cyclic flexural strains. For this purpose, the FE models of the HP220x57 SHP specimens are subjected to constant amplitude cyclic flexural strain with amplitude of ε_a=2.5ε_y, 5ε_y, 7.5ε_y 10ε_y and 15ε_y at the extreme fibers of the flanges in the absence and presence of axial loads where the axial loads are taken as 0.05P_y, 0.075P_y, 0.11P_y, 0.16P_y and 0.20P_y. The analyses results are summarized in Table 6 and graphically presented in Figs. 26 and 27.

Fig. 26 shows the number of cycles to failure (LCF life) as a function of the flexural strain amplitude. As expected, the number of cycles to failure is inversely proportional to the strain amplitude. Furthermore, Fig. 26 shows that as the axial load level increases, the LCF life dramatically decreases beyond a certain constant amplitude strain level. This may be explained as follows; the combination of large axial loads with large amplitude flexural strain cycles results in considerable local buckling of the flanges of the SHP specimen and associated large misalignment of the buckled plate.

Table 6 FE analysis results for HP220x57 steel section oriented along the strong axis

Section Type	Load Type	Test Number	Axial load	Strain Amplitude (ε_a)	Number of Cycles to Fracture
HP 220x57 Strong Axis	*No Axial Load*	1	P=0	1.5ε_y	3672
		2		2.5ε_y	2198
		3		5ε_y	205
		4		7.5ε_y	191
		5		10ε_y	167
		6		15ε_y	58
	Axial + Longitudinal direction load	7	P=0.05P_y	2.5ε_y	2294
		8	P=0.075P_y		2332
		9	P=0.11P_y		4238
		10	P=0.16P_y		6732
		11	P=0.20P_y		7115
		12	P=0.05P_y	5ε_y	278
		13	P=0.075P_y		319
		14	P=0.11P_y		585
		15	P=0.16P_y		825
		16	P=0.20P_y		918
		17	P=0.05P_y	10ε_y	122
		18	P=0.075P_y		98
		19	P=0.11P_y		67
		20	P=0.16P_y		41
		21	P=0.20P_y		23
		22	P=0.05P_y	15ε_y	43
		23	P=0.075P_y		31
		24	P=0.11P_y		20
		25	P=0.16P_y		13
		26	P=0.20P_y		5

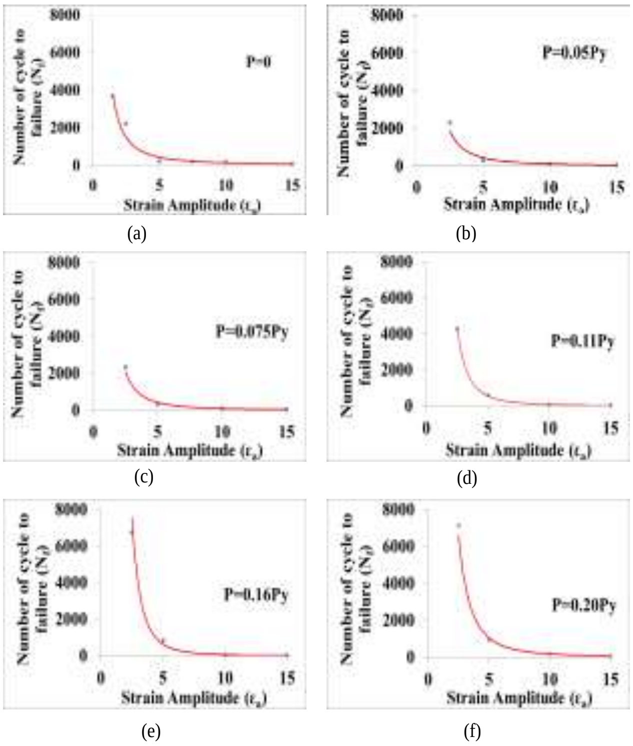

Fig. 26 Number of cycle to failure versus strain amplitude for HP220X57 section; (a) P=0.P_y, (b) P=0.05P_y, (c) P=0.075P_y, (d) P=0.11P_y, (e) P=0.16P_y and (f) P=0.20P_y in FEM

Consequently, applying a compressive axial load on the pile specimen produces additional second order effects due to the large misalignment of the already buckled flange plate leading to more exaggerated buckling of the flange. This, in turn, leads to large strain concentrations that accelerates the crack growth and associated reduction in the LCF life of the SHP specimen. This has been confirmed experimentally by an earlier research study (Karalar and Dicleli).

Fig. 27 shows the number of cycles to failure as a function of axial load for various levels of constant amplitude strain. From the figure, the axial load is observed to have a significant effect on the LCF performance of steel H-piles. For cyclic strain amplitudes smaller than and equal to 5εy, the axial load is observed to have a positive effect on the LCF life of the SHP. That is, the LCF life increases with increasing levels of axial loads and the relationship between the LCF life and the axial load is linear. However for cyclic strain amplitudes larger than 5εy, the axial load is observed to have an adverse effect on the LCF life of the SHP. For such large cyclic strain amplitudes, the LCF life becomes inversely proportional to the axial load. As explained earlier this is due to the exaggerated local buckling of the flanges when large cyclic strain amplitudes are combined with large axial load levels.

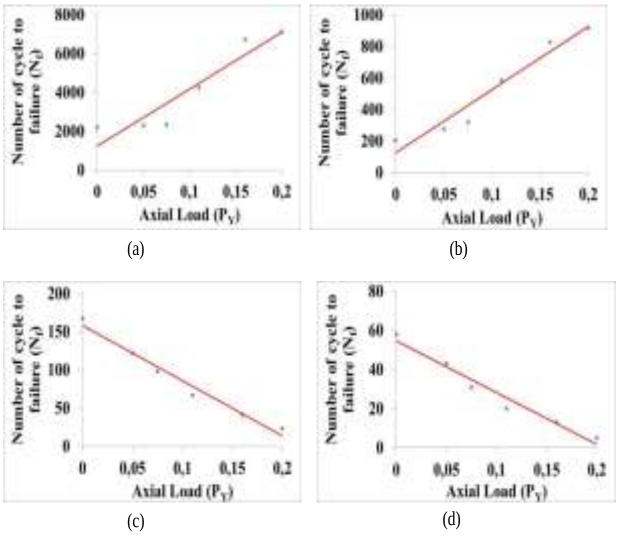

Fig. 27 Number of cycle to failure versus Axial load (Py) for HP220X57 section; (a) 2.5ε_y, (b) 5ε_y, (c) 10ε_y and (d) 15ε_y in FEM

10. Conclusions

In this research study, the potential of using FE modeling techniques to estimate the LCF life of SHPs commonly used in IABs is investigated. For this purpose, first, experimental tests are conducted on several SHP specimens to determine their LCF life under thermal-induced cyclic flexural strains where the specimens are subjected to longitudinal displacements / flexural strains with various amplitudes in the absence and presence of typical axial loads. Next, nonlinear FE models of the tested SHP specimens are developed using the computer program ANSYS to predict the LCF life of the tested SHPs.

The experimental test results revealed that LCF lives of piles with different sizes subjected to identical cyclic flexural strains at the extreme fibers of the flanges are nearly identical. This is expected, as the number of cycles to failure is a function of the amplitude of the cyclic strain according to the Coffin-Manson's relationship. As the tested SHP specimens are not made of compact sections, in all the cases, local buckling of the flanges of the HP sections occurred with larger local buckling effects at larger cyclic flexural strain amplitudes. It is also observed that the LCF life of the SHP specimens increases due to the presence of axial load. The axial load, in these specific cases, has a positive impact on the LCF performance of the SHPs. This is expected as the axial load produces axial compressive strains within the entire pile cross-section that tend to slow down the fatigue crack propagation due to tensile strains. Thus, larger axial load resulted in larger number of cycles to failure. However, the behavior of piles under large amplitude strains in the presence of axial load may be different.

The comparison of FE analysis results with the experimental test results revealed that the FE models of the tested SHP specimens predicted the LCF life of the SHP specimens, the location of fatigue cracks, strains at various locations on the SHPs, the deformed shape of the SHP specimens as well as local buckling in the flanges of the SHP specimens reasonably well. This clearly indicates that FE simulation may be an excellent alternative for destructive laboratory tests with acceptable variations in the results. Thus, FE simulation may effectively be used to predict the actual behavior of SHPs in IABs under thermal-induced cyclic longitudinal displacements and axial loading.

Furthermore, a parametric study is conducted using the FE models of the SHP specimens to obtain a relationship between the LCF life and flexural strain amplitude for various levels of axial loads as well as a relationship between the LCF life and axial load for various levels of cyclic flexural strains. The axial load is observed to have a significant effect on the LCF performance of steel H-piles. For cyclic strain amplitudes smaller than and equal to 5εy, the axial load is observed to have a positive effect on the LCF life of the SHP. That is, the LCF life increases with increasing levels of axial loads and the relationship between the LCF life and the axial load is linear. However, for cyclic strain amplitudes larger than 5εy, the axial load is observed to have an adverse effect on the LCF life of the SHP. For such large cyclic strain amplitudes, the LCF life becomes inversely proportional to the axial load. This is mainly due to the exaggerated local buckling of the flanges when large cyclic strain amplitudes are combined with large axial load levels. This, in turn, leads to large strain concentrations that accelerates the crack growth and associated reduction in the LCF life of the SHP specimen.

References

AASHTO (2017), LRFD Bridge Design Specification

ANSYS (1998), ANSYS, Inc., Canonsburg, Pennsylvania.

Arsoy, S., Duncan, J.M. and Barker, R.M. (2001), Experimental and Analytical Investigations of Piles and Abutments of Integral Bridges, Contract Report, Department of Civil and Environmental Engineering Virginia Polytechnic Institute and State University.

ASTM (2005), Standard Test Methods for Tension Testing of Metallic Materials.

Azamfar, M. and Moshrefifar, M. (2014), "Moshrefifar and Azamfar method, a new cycle counting method for evaluating fatigue life", *Int. J. Fatigue*; **69**, 2-15. https://doi.org/10.1016/j.ijfatigue.2014.03.020.

Chocichien Voraniti (2004), The Behavior and Design of Piles for Integral Abutment Brıdges, Ph.D thesis.

Coffin, L.F. (1954), "A study of the effects of cyclic thermal stresses on a ductile metal", *T. Am. Soc. Mech. Eng*., 931-950.

Dicleli, M. (2000), "A rational design approach for prestressed-concrete-girder integral bridges", *Eng. Struct*., **22**(3), 230-245. https://doi.org/10.1016/S0141-0296(98)00080-7.

Dicleli, M. and Albhaisi, S.M. (2004), "Effect of cyclic thermal loading on the performance of steel H-Piles in integral bridges with stub-abutments", *J. Constr. Steel Res*.; **60**(2):161-182. https://doi.org/10.1016/j.jcsr.2003.09.003.

Dicleli, M. and Calik, E.E. (2008), "Physical theory hysteretic model for steel braces", *J. Struct. Eng. ASCE*, **134**(7), 1215-1228. https://doi.org/10.1061/(ASCE)0733-9445(2008)134:7(1215).

French, C., Huang, J. and Shield, C. (2004), Behavior of Concrete Integral Abutment Bridges, Final Report.

Frosch, R.J., Chovichien, V., Durbin, K. and Fedroff, D. (2006), Jointless and Smoother Bridges: Behavior and Design of Piles, Joint Transportation Research Program Technical Report Series.

Haliburton, T.A. (1971), Soil structure interaction; numerical analysis of beams and beam columns, Technical Publication No. 14, School of Civil Engineering, Oklahoma State University, Stillwater, Oklahoma.

Hällmark, R. (2006), Low Cycle Fatigue of Steel Piles in Integral Abutment Bridges, Master Thesis.

Huang, J., French, C. and Shield, C. (2004), Behavior of concrete integral abutment bridges., Final Report. Minnesota Department of Transportation, Research Service Section.

Kadhim, M.M.A. (2012), Factors effect on the effective length in a double strap joint between steel plates and CFRP, Vol.1, 11-18.

Kamil, J.A. Khan, I.A. and Nath, Y. (2011), Numerical and Experimental Dynamic Contact of Rotating Spur Gear, Vol. 5, 254-263.

Karalar, M. and Dicleli, M. (2016), "Effect of thermal induced flexural strain cycles on the low cycle fatigue performance of integral bridge steel H-piles", *Eng. Struct*., **124**, 388-404. https://doi.org/10.1016/j.engstruct.2016.06.031.

Karalar, M. and Dicleli, M. (in-print) "Fatigue in jointless bridge H-piles under axial load and thermal movements", *J, Constr, Steel Res*..

Karthigeyan, S., Ramakrishna, T and Karpurapu, R. (2006), "Influence of vertical load on the lateral response of piles in sand", *Comput. Geotechnics*, **33**(2), 121-131. https://doi.org/10.1016/j.compgeo.2005.12.002.

.Khodair, Y.A. and Hassiotis, S. (2005), "Analysis of soil-pile interaction in integral abutment", *Comput. Geotechnics*, **32**(3), 201-209. https://doi.org/10.1016/j.compgeo.2005.01.005.

Khodair, Y.A. and Hassiotis, S. (2013), "Numerical and experimental analyses of an integral bridge", *Int. J. Adv. Struct. Eng.*, **5**, 14.

Manson, S.S. (1954), Behavior of Materials Under Conditions of Thermal Stress. National Advisory Commission on Aeronautics: Report 1170, Cleveland, Lewis Flight Propulsion Laboratory.

Razmia, J., Ladanib, L. and Aggoura, S.M. (2014), "Finite element simulation of pile behavior under thermo-mechanical loading in integral abutment bridges", *Struct. Infrastruct. Eng*., **10**(5), 643-665.

SAP2000 (2016), Integrated finite element analysis and design of structures. Computers and Structures Inc., Berkeley, California.

Stephens, R.I., Fatemi, A., Stephens, R.R. and Fuchs, H.O. (2000), Metal Fatigue in Engineering.

Suresh, S. (2004), Fatigue of Materials, Cambridge University Press.

Virdi, K.S., Matthews, R.S., Clarke, J.L. and Garas, F.K. (2000), Abnormal Loading on Structures: Experimental and Numerical Modelling, E & FN Spon, London.

Wiss, J. (2002), Synthesis of Technical Information for Jointless Bridge Construction, Technical Report, Elstner Associates, Inc., State of Vermont Agency of Transportation, 25-36, June.

Xiao, Y. and Chen, L. (2013), "Behavior of model steel H-pile-to-cap connections", *J. Constr. Steel Res*., **80**, 153-162. https://doi.org/10.1016/j.jcsr.2012.09.008.

Xiao, Y., Wu, H., Yaprak, T.T., Martin, G.R. and Mander J.B. (2006), "Experimental studies on seismic behavior of steel pile to pile cap connections", *J. Bridge Eng*., **11**(2), https://doi.org/10.1061/(ASCE)1084-0702(2006)11:2(151).

BU